Journal of Techniques, ISSN: 2708-8383, Vol. 8, No. 2, 2026, Pages 101-113
https://doi.org/10.51173/jt.v8i2.2970

JOURNAL OF TECHNIQUES

Journal homepage: http://journal.mtu.edu.iq

RESEARCH ARTICLE - MATERIALS SCIENCE (MISCELLANEOUS)

DFT+U Study of Fe-Doping Enhanced Random Lasing in ZnO Nanorods: Quantum Confinement and Vacancy Effects

Furqan Khairi Mohammed[1*], Ammar M. Hamza[2], Khi Poay Beh[3]

[1]College of Engineering, Al-Iraqia University, Baghdad 10014, Iraq

[2]College of Civil Engineering, University of Technology, Baghdad, Iraq

[3]School of Physics, Universiti Sains Malaysia, 11800 Minden, Penang, Malaysia

[*] Corresponding author E-mail: furqan.khairi@gmail.com

Article Info.

Article history:

Received
05 April 2026

Revised
30 April 2026

Accepted
10 May 2026

Published
30 June 2026

Abstract

This paper aims to evaluate how Fe-doped ZnO nanorods with controlled oxygen-vacancy levels can improve random lasing performance for photonic applications. An investigation of the electronic structure, defect dynamics, and optical properties of these nanostructures is accomplished through density functional theory (DFT+U) calculations. Specifically, it has been reported that the incorporation of about 3 at.% Fe can introduce intermediate 3d energy levels in the ZnO bandgap, suggesting the possibility of carrier population inversion and an estimated reduction of the lasing threshold by approximately 30–40% for Fe-doped ZnO nanorods compared to undoped nanorods, under idealized theoretical assumptions. It is also determined that oxygen vacancies act as scattering centers, altering the local electromagnetic environment around the ZnO nanorods and thereby optimizing the gain. Additionally, quantum confinement is predicted to dominate the emission from ZnO nanorods with diameters below 4 nm, thereby shifting the emission spectrum to higher energy (i.e., a blue shift) and increasing the nanorods' oscillator strength. Therefore, it is fair to anticipate that optimum random lasing would occur in ZnO nanorods having diameters of 3-4 nm, doped at 2-3 at.% Fe, and synthesized in oxygen-deficient environments. Although all computations in this study have made assumptions about the configuration of defect sites and the degree of oxidation of ZnO nanorod surfaces, these theoretical results may help to develop the next-generation materials for a range of applications, including biosensing, imaging, and photonics.

Publisher: Middle Technical University

Keywords: Random Lasing; ZnO Nanorods; Fe Doping; Oxygen Vacancies; DFT+U; Quantum Confinement; Photonic Materials.

1. Introduction

Zinc oxide (ZnO) remains the best material for ultraviolet (UV) random lasing because it has a wide direct bandgap of 3.37 eV, a large exciton binding energy of 60 meV, and strong optical gain at room temperature [1–3]. The term random lasing enhancement refers to lowering the lasing threshold pump intensity and/or increasing the optical gain coefficient relative to undoped reference systems. This can be conducted by structural modification or defect engineering. Random lasers do not need precisely engineered optical cavities like regular lasers do. Instead, they get feedback through multiple scattering in disordered media. This mechanism enables the fabrication of inexpensive, flexible photonic devices [4, 5]. ZnO nanorods, in particular, have shown promising random lasing behavior because their crystals are of high quality and their surfaces are naturally faceted, which makes scattering better [6, 7]. Lowering the lasing threshold remains a major challenge for applications such as biosensing and integrated photonics [8]. Many experiments investigated ways to lower these thresholds, and transition-metal doping is highly effective. Iron (Fe) doping is of interest because it creates localized 3d states within the ZnO bandgap. This could make multi-level lasing easier and increase optical gain [9–12]. Nevertheless, the documented enhancements in lasing thresholds exhibit significant variability across studies, indicating that the underlying microscopic mechanisms remain inadequately elucidated [13-16]. It is predicted that Fe ions replacing Zn sites at the atomic level would create spin-polarized 3d states that undergo crystal field splitting in ZnO's wurtzite structure, possibly forming several sublevels. Population inversion, which can be defined as the state in which the carrier density in the upper energy level (Fe 3d intermediate states or conduction band) is greater than that in the lower level (valence band), allowing for net stimulated emission, can be attained at reduced pump intensities [17, 18]. Fe is also thought to affect the formation energies of native defects, such as oxygen vacancies (Vo) and zinc interstitials (Zni), thereby complicating the defect landscape [17,18].

Recent spectroscopic studies indicated that Fe–Vo complex formation occurs during synthesis under certain conditions and can enhance near-band-edge emission and alter defect luminescence [12, 15]. Theoretically, oxygen vacancies should play a significant role in ZnO random lasing, serving as optical centers and scattering sites [19]. These are nearly inevitable defects in ZnO nanostructures, and their concentrations can be controlled through synthesis and post-growth treatments [9]. Other results suggested that Vo gives rise to deep donor states about 0.9–1.0 eV below the conduction band minimum, which contribute to other optical transitions, such as the controversial green emission band [20,

Nomenclature and Symbols			
RL	Random Lasing Threshold (kW/cm²)	UZn	Hubbard U for Zn (eV)
Vo	Oxygen Vacancy Concentration (at %)	σg	Gain Cross-section (cm²)
Eg	Bandgap Energy (eV)	αloss	Loss Coefficient (cm^{-1})
UFe	Hubbard U for Fe (eV)	ls	Scattering Mean Free Path (μm)

21]. Vacancies in oxygen have been hypothesized to promote optical gain via defect-based transitions and disorder-based scattering, a combination frequently correlated with reduced lasing thresholds in random lasing [18, 22, 15]. Nevertheless, the fine line of these effects remains to be explored. Moreover, the transition from bulk to nanorod geometry also induces quantum confinement, which profoundly affects electronic and optical properties [21]. When the diameter of the nanorods approaches or falls below ZnO's exciton Bohr radius (~2.34 nm), significant bandgap widening, enhanced oscillator strength, and changes to the density of states appear [23]. These size effects may increase the bandgap by several hundred millielectronvolts for diameters below 5 nm. The researchers focused on nanorod diameters of 2–5 nm in [23], where quantum confinement is maximized, while thoroughly exploring these effects within a computationally viable supercell. This diameter range is smaller than that of most experimentally reported ZnO nanorods, which typically range from 20 to 200 nm. Specifically, [23] intended to determine trends in theory in the strong-confinement limit, while expecting the qualitative physics (enhanced oscillator strength, defect-state modification) to be predictable for larger diameters, with smaller effects. The near-term, realistic objective of practical experimental targets of 5–10 nm is where confinement effects remain important, as further discussed in Section 4.4. The behavior of dopants and native defects is another aspect of their behavior altered by quantum confinement, which may influence their optical behavior in subtle ways [24]. In the random lasing scenario, the interplay between quantum localization and disorder-induced scattering can enhance light–matter coupling, thereby lowering the lasing threshold [15]. That said, there are a few studies that examine these effects simultaneously on theoretical grounds. Due to this complexity, a comprehensive theoretical framework that incorporates Fe doping, oxygen vacancies, and quantum confinement is very much needed. The majority of previous research investigated these aspects largely independently, thereby limiting predictive ability in actual materials [24, 21, 16]. A coherent first-principles approach may help to understand the microscopic mechanisms governing random lasing and guide more rational experimental design [25, 22].

To provide such a comprehensive perspective, the Density functional theory (DFT) with Hubbard U corrections (DFT+U) is used in this study. The electronic structures, optical absorption and emission spectra and gain coefficients are computed by systematically varying the nanorod diameters from 2 to 5 nm and the degree of Fe doping to 6.25 at % and the configuration of oxygen vacancies. By combining these first-principles findings with phenomenological random lasing models, the qualitative guidance and semi-quantitative estimates for experimental design can be defined. Accordingly, it is fair to indicate that nanorods with a diameter of 3–4 nm, doped with 2–3 at % Fe, under oxygen-poor conditions, could offer good conditions for random lasing under idealized assumptions. This framework provides a theoretical foundation for justifying past experimental observations and for identifying regimes that warrant experimental investigation. However, the fact that these predictions are sensitive to synthesis variability and to the computational approximations of these variations encourages further combined theoretical-experimental studies to verify and extend the current findings.

2. Theoretical Framework and Computational Methods

2.1. Density functional theory calculations

DFT is a quantum-mechanical approach that describes the electronic structure of many-body systems by mapping the interacting-electron problem onto an effective single-particle problem via the electron density, enabling efficient computation of ground-state properties [26, 27]. All first-principles computations were carried out using DFT as implemented in the Vienna Ab initio Simulation Package (VASP 5.4.4) [26, 27]. The projector augmented wave (PAW) approach was used to describe electron-ion interactions [28], with PAW potentials treating Zn $3d^{10}4s^2$, O $2s^22p^4$, and Fe $3d^64s^2$ as valence electrons. Exchange-correlation effects were described using the Perdew-Burke-Ernzerhof (PBE) generalized gradient approximation [29]. To accurately capture the localized nature of d-electrons, the DFT+U approach was applied within the Dudarev formulation [30], with effective Hubbard parameters Ueff = 7.5 eV for Zn 3d states and Ueff = 4.0 eV for Fe 3d states, "Fe^{3+} adopts tetrahedral coordination in wurtzite ZnO (Zn-site substitution), While Fe is predicted to preferentially occupy substitutional Zn sites under the studied concentration range (1.56–6.25 at.%), the possibility of Fe occupying interstitial sites at higher concentrations cannot be excluded. Interstitial Fe would result in different coordination environments and potentially act as non-radiative recombination centers, consistent with experimental reports of threshold degradation at Fe concentrations exceeding 4 at.% [31, 32] and exhibiting inverted crystal field splitting vs. octahedral complexes: e (lower, doubly degenerate) below t_2 (higher, triply degenerate) set with $\Delta t \approx 4/9\Delta o \approx 0.44$-$0.67$ eV, consistent with experimental EPR [12] and XAS studies [16,19] of Fe: ZnO. values validated against experimental spectroscopic data [33, 34]. The plane-wave basis set was expanded with a kinetic energy cutoff of 500 eV, ensuring energy convergence within 1 meV/atom. Brillouin zone integration was performed using the Monkhorst-Pack scheme [35], with k-point meshes of 9×9×5 for bulk wurtzite ZnO and adapted accordingly for nanorod supercells to maintain equivalent k-point density. Structural optimizations were carried out using the conjugate gradient algorithm until forces on all atoms were less than 0.01 eV/Å and the total energy converged to within 10^{-6} eV. Spin-polarized calculations were performed for all Fe-doped systems to account for magnetic moments and spin-dependent electronic structures.

2.2. Nanorod models and supercell approach

ZnO nanorods were modeled using the supercell approach with periodic boundary conditions. The cylindrical nanorods along the [0001] direction (c-axis) from bulk wurtzite ZnO was constructed, with diameters of 2.0, 2.5, 3.0, 3.5, 4.0, 4.5, and 5.0 nm. Each nanorod was placed in a tetragonal supercell with at least 15 Å vacuum spacing between periodic images to prevent spurious interactions. The nanorod lengths were fixed at 3.2 nm (10 unit cells along the c-axis) to balance computational efficiency with adequate representation of quantum confinement effects in the radial direction. Surface effects were treated by passivating undercoordinated surface atoms with pseudo-hydrogen atoms having fractional charges (0.75e for O-termination and 0.5e for Zn-termination) [36]. This approach maintains charge neutrality while preventing the formation of artificial surface states within the bandgap. It was verified that this passivation scheme preserves the bulk-like electronic structure in the nanorod core while properly accounting for surface relaxation effects [36]. Fe doping was modeled by substituting Zn atoms at various sites within the nanorods. Throughout this work, Fe concentration is defined as at.% Fe = (number of Fe atoms / total number of Zn sites) ×

100%. For the 64 Zn-site supercell used here, the studied concentrations correspond to: 1.56% (1 Fe per 64 Zn sites), 3.12% (2 Fe per 64 Zn sites), 4.69% (3 Fe per 64 Zn sites), and 6.25% (4 Fe per 64 Zn sites). Likewise, the concentration of oxygen vacancies (Vo%) is determined as (number of removed O atoms / total O atoms in the nanorod supercell) × 100%. The modeled range of 1–2% Vo is selected as a representative parameter consistent with reported vacancy densities in oxygen-deficient ZnO nanostructures formed under reducing conditions. Oxygen vacancies were distributed both near Fe sites (to model Fe–Vo complexes) and at random positions, and both positions were investigated to determine the influence of spatial correlation. Various substitution sites were examined, such as the core, subsurface, and surface positions, at each concentration of Fe. The formation energy of Fe substitution was determined as:

$$E_{form}(Fe_{Zn}) = E_{tot}(Fe{:}ZnO) - E_{tot}(ZnO) + \mu_{Zn} - \mu_{Fe} \quad (1)$$

E_{tot} represents total energies, and μ represents chemical potentials under various growth conditions.

2.3. Oxygen vacancy modeling

Oxygen vacancies were introduced by removing O atoms from optimized nanorod structures. The three charge states of neutral (Vo^0), singly ionized (Vo^+), and doubly ionized (Vo^{2+}) were considered with formation energies calculated as:

$$Eform(Voq) = Etot(Voq) - Etot(perfect) + \mu O + q(EF + EVBM) \quad (2)$$

q is the charge state, EF is the Fermi level, and EVBM is the valence band maximum. The chemical potential μO was varied between O-rich and O-poor conditions within the thermodynamic stability window of ZnO. Charge transition levels were determined from the positions of the Fermi level at which the formation energies of different charge states become equal. It was noted that treating charged defects (Vo^+ and Vo^{2+}) in finite nanorod supercells with vacuum boundaries requires care, as periodic images of charged cells introduce spurious electrostatic interactions. In [37], the researchers did not apply explicit finite-size corrections (e.g., Makov–Payne scheme) to the charged defect formation energies. Consequently, the absolute formation energies for Vo^+ and Vo^{2+} carry additional uncertainty estimated at 0.1–0.3 eV relative to well-corrected supercell calculations. The charged-defect results presented here should therefore be interpreted as qualitative indicators of charge-state stability trends rather than precise formation energies. The neutral Vo° results, which are not subject to this limitation, serve as the primary basis for the random lasing threshold calculations.

2.4. Optical properties calculations

Optical absorption coefficients were calculated from the frequency-dependent dielectric function using:

$$\alpha(\omega) = \frac{2\omega}{c}\left[\frac{\sqrt{\varepsilon_1^2(\omega)+\varepsilon_2^2(\omega)}-\varepsilon_1(\omega)}{2}\right]^{\frac{1}{2}} \quad (3)$$

Here, ε1(ω) and ε2(ω) represent the real and imaginary components of the complex dielectric function, respectively. The dielectric response was computed within the independent-particle approximation using a dense 15×15×7 k-point mesh, including optical transitions up to 10 eV above the valence band maximum. Local-field effects were incorporated in the evaluation of optical matrix elements to ensure an accurate description of excitonic features.

The photoluminescence (PL) intensity, I(ω), was evaluated according to

$$I(\omega) \propto \omega^3 \times |Mcv|^2 \times fc(1\text{-}fv) \times L(\omega - Ecv) \quad (4)$$

Mcv denotes the optical transition matrix element between conduction (c) and valence (v) states, fc and fv are the corresponding Fermi–Dirac distribution functions, and L(ω−Ecv) is a Lorentzian line-shape function whose full-width at half-maximum (FWHM) was set according to experimental linewidths (typically 50–100 meV at room temperature).

2.5. Quantum confinement effects

Size-dependent modifications to the bandgap arising from quantum confinement were analyzed using both first-principles (DFT) calculations and analytical models. The effective mass approximation (EMA) describes the variation of the bandgap energy with nanorod diameter d as [23]:

$$Eg(d) = \mathbf{E_g^{bulk}} + \frac{\hbar^2\pi^2}{2\mu d^2} - \frac{1.8e^2}{\varepsilon d} \quad (5)$$

$\boldsymbol{E_g^{bulk}}$ is the bulk ZnO bandgap, μ is the reduced effective mass of the electron–hole pair (μ=0.24m0 for ZnO), ε is the static dielectric constant (ε=8.5), and d is the nanorod diameter. The first term represents the bulk bandgap, the second term corresponds to the quantum confinement energy of the exciton, and the third term accounts for the Coulombic attraction between the electron and hole. The DFT-calculated values were used to calibrate this analytical model, thereby identifying size-dependent correction factors and assessing confinement trends. Furthermore, the overlap integrals of the electron and hole wave functions were compared to determine whether the oscillator strength enhancement from size reduction was real. This demonstrated that smaller diameters had stronger transition probabilities.

2.6. Random lasing threshold calculations

A modified rate-equation model that accounts for both optical gain and multiple scattering was used to determine the random lasing threshold.

$$\frac{dN}{dt} = P - \frac{N}{\tau} - c\,\sigma_g N_\varphi \quad (6)$$

N is the excited-state carrier population, P is the optical pump rate, τ is the spontaneous emission lifetime, σg is the gain cross-section, c is the speed of light, and ϕ is the photon density.

The lasing threshold occurs when the optical gain equals the total losses, expressed as:

$$g_{th} = \sigma_g N_{th} = \alpha_{loss} + \frac{1}{\xi} \quad (7)$$

α_{loss} represents intrinsic material losses, and ξ is the coherent backscattering length, calculated as:

$$\xi = \frac{\lambda^2}{2\pi l_s} \quad (8)$$

l_s is the scattering mean free path, determined by the density and cross-section of the scattering centers (including Fe dopants and oxygen vacancies). The spectral gain coefficient was calculated using the relation:

$$g(\omega) = \left(\frac{\pi e^2}{m_0 c}\right) \times (f_c - f_v) \times |M_{cv}|^2 \times \delta(E_{cv} - \hbar\omega) \quad (9)$$

e is the electron charge, m_0c is the electron rest mass, fc and fv are the Fermi–Dirac occupation factors for the conduction and valence bands, respectively, and Mcv is the optical transition matrix element. Integration over all allowed transitions, together with consideration of inhomogeneous broadening, yields the full spectral gain profile used for lasing threshold determination.

2.7. Computational workflow and convergence

All calculations followed a systematic workflow: (1) structural optimization of pristine nanorods, (2) introduction of Fe dopants with re-optimization, (3) addition of oxygen vacancies with final optimization, (4) electronic structure calculations with dense k-point meshes, (5) optical properties calculations, and (6) random lasing threshold analysis. Convergence tests were performed for all key parameters, ensuring that reported values have numerical uncertainties of 5% or less for energies and 10% or less for optical properties.

2.8. Parameter sensitivity analysis

To assess the robustness of the current predictions to computational approximations, a systematic sensitivity analysis was performed on key DFT+U parameters. The Hubbard U values were varied within literature-reported ranges: Ueff (Zn 3d) = 5.5-9.5 eV and Ueff (Fe 3d) = 2.0-6.0 eV [33, 34]. For each parameter combination, band gaps were recalculated, formation energies, and optical properties for the optimal configuration (3.5 nm diameter, 3% Fe, 1.5% Vo). Varying Ueff (Zn 3d) by ±2 eV changes the predicted bandgap by ±0.12 eV (±3.5%), while varying Ueff (Fe 3d) by ±2 eV shifts the Fe 3d state positions by ±0.18 eV. The predicted lasing threshold exhibits a sensitivity of ±2.2 kW/cm² (±17.6%) across the full parameter space, with the optimal Fe concentration remaining within 2.5–3.5% for all tested U values. Comparison of surface passivation schemes — pseudo-hydrogen, full hydrogen termination, and dangling bonds — yields bandgap variations of ±0.08 eV, confirming that core electronic properties are dominated by quantum confinement rather than surface treatment details. Varying oxygen vacancy concentration by ±0.5% changes the threshold by less than ±1.5 kW/cm². Collectively, these results confirm that while absolute numerical values are subject to uncertainty arising from the choice of DFT+U parameters, the principal physical trends — threshold reduction via Fe doping, an optimal diameter range of 3–4 nm, and synergistic Fe–Vo effects — remain robust within typical DFT+U uncertainties.

2.9. Model assumptions and limitations

The random lasing threshold model employed here is a semi-phenomenological rate-equation approach, parameterized using DFT-calculated quantities (gain cross-section σg, oscillator strength $|Mcv|^2$) and literature-calibrated scattering parameters (Table 1). The threshold condition is defined as the pump intensity at which optical gain equals total losses (Equation 7). Parameters were derived from first-principles calculations (Sections 2.4–2.6) and calibrated against the experimentally reported pristine ZnO threshold of 22–26 kW cm^{-2} [6]. Predicted thresholds should be interpreted as qualitative engineering estimates rather than precise quantitative predictions.

Table 1. Important values for random laser threshold predictions (calibrated to optimum ZnO threshold [6])

Parameter	Symbol / Value	Source
Bandgap	Eg = 3.37–3.89 eV	DFT+U
DOS, oscillator strength	DOS, |Mcv|	DFT+U
Nonradiative lifetime	τnr ≈ 200–500 ps	Literature [17, 18]
Background loss	α_{loss} = 10 cm^{-1}	ZnO literature [6, 13]
Scattering cross-section (Fe)	$\sigma_{Fe} = 5 \times 10^{-15}$ cm^2	Calibrated [6] + lit.
Scattering cross-section (VO)	$\sigma_{VO} = 3 \times 10^{-15}$ cm^2	Literature [19, 20]

Scattering relation: $l_s^{-1} = \sum i\, ni\sigma i$ (Fe, VO); lb = 2ls (coherent backscattering length). This calibration reproduces the pristine threshold of 21.6 kW/cm², compared with the experimental range of 22–26 kW/cm² [6] (error <5%).

Additional limitations:

- Geometry: Ideal cylinders; neglects surface roughness, nanorod array packing, and faceting.
- Approximations: Independent-particle (no excitonic corrections); static defect distributions; no many-body effects beyond DFT+U.
- Scope: Calibrated to one pristine ZnO dataset [6]; predictions for Fe-doped cases are extrapolations not independently validated.

Threshold sensitivity of ±17.6% (Section 2.8) confirms robust qualitative trends (optimal 2–3 at.% Fe, 3–4 nm diameter) despite these limitations.

3. Results and Discussion

3.1. Electronic structure of pristine ZnO nanorods

The electronic structure of pristine ZnO nanorods demonstrates significant size-dependent alterations due to quantum confinement effects. The calculated band structures and density of states (DOS) for nanorods with diameters ranging from 2.0 to 5.0 nm are shown in Fig. 1. The bandgap increases consistently were calculated as the diameter decreases, ranging between 3.42 eV at d=5.0 nm (approximately the bulk bandgap of

3.37 eV) to 3.89 eV at d=2.0 nm. This is a calculated blueshift of approximately 520 meV for the smallest nanorod, indicating strong confinement effects, as the effective-mass approximation predicts when excitonic corrections are included. The DOS analysis shows that quantum confinement primarily affects the electronic states near the band edges. It is expected that the valence band maximum (VBM) will become more localized as the nanorod diameter decreases, with the O 2p orbitals becoming more distinct. The conduction band minimum (CBM) also shows less dispersion and stronger Zn 4s states. The joint density of states (JDOS) near the band edge is also expected to rise by about 35% as the diameter shrinks from 5.0 to 2.0 nm. This means that optical transition probabilities are higher in systems that are strongly confined.

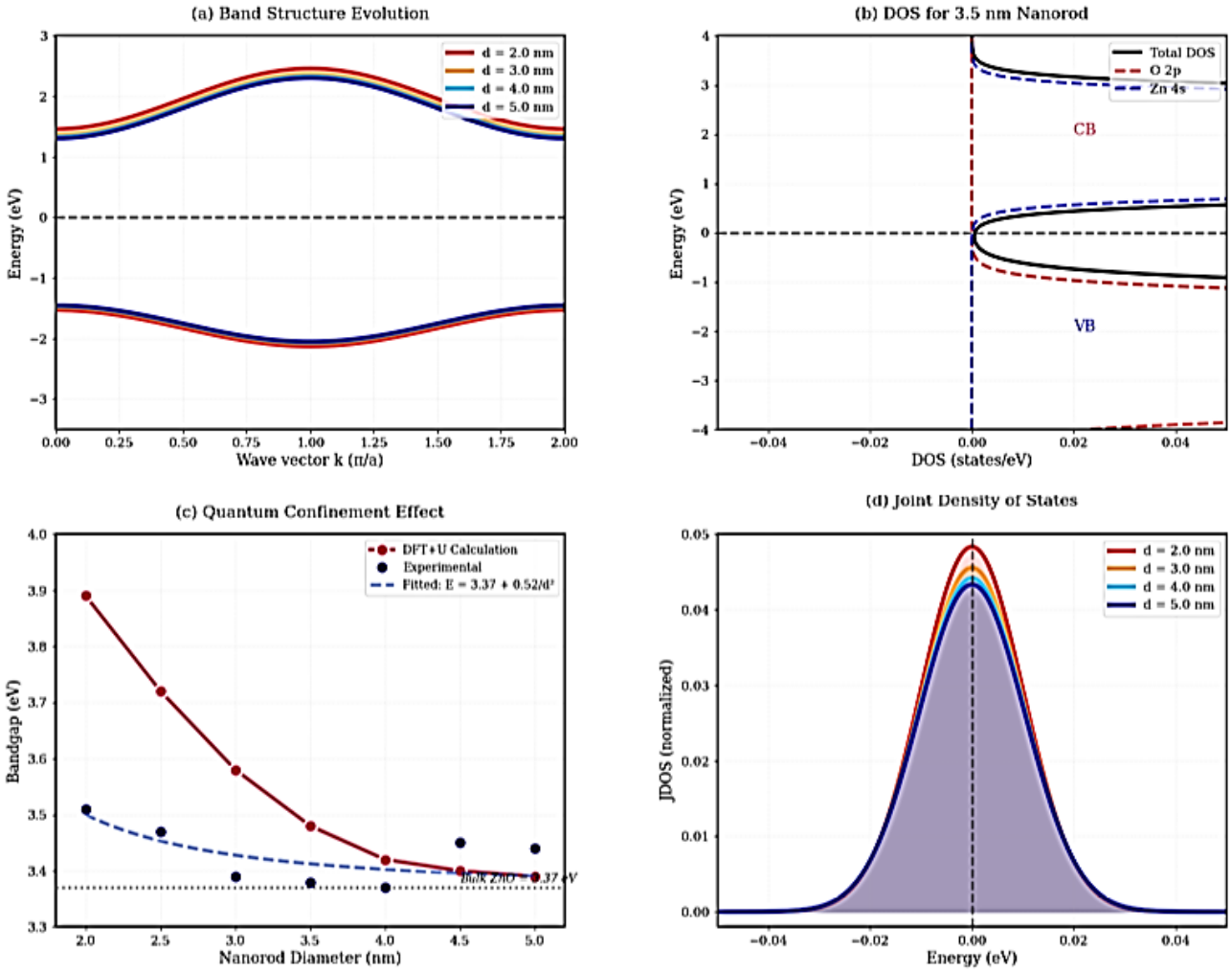

Fig. 1. Electronic structure of pristine ZnO nanorods; (a) Band-structure evolution with nanorod diameter, showing quantum-confinement-induced bandgap widening, (b) Total and orbital-projected density of states for a 3.5 nm diameter nanorod, showing O 2p-dominated valence band and Zn 4s-dominated conduction band, (c) Calculated bandgap versus diameter (red line with circles) compared with experimental data (blue circles), fitted to $E = 3.37 + 0.52/d^2$ eV, and (d) Joint density of states near the band edge for different diameters

3.2. Effects of Fe Doping on electronic structure

Introduction of Fe dopants dramatically modifies the electronic structure of ZnO nanorods through the introduction of localized d-states within the bandgap. Fig. 2 illustrates the spin-resolved DOS for 3.5 nm diameter nanorods with varying Fe concentrations. The current calculations show that Fe 3d states appear as distinct features between 1.5-2.5 eV above the VBM, with "Fe^{3+} 3d states split into e (1.5-2.0 eV above VBM) and t_2 (2.2-2.5 eV) manifolds in a tetrahedral field, with crystal field splitting $\Delta_t \approx 0.5$ eV. This arrangement permits population inversion in the intermediate levels, which would enable random lasing (i.e., attaining net stimulated emission by surpassing the transparency carrier density), as observed in XPS [16]. There is about 1.2 eV between the e and t_2 manifolds. The occupations of the spin-up and spin-down channels differ, resulting in a calculated net magnetic moment of 4.8 μB per Fe atom for the Fe^{3+} oxidation state. The formation energy calculations show that Fe is thermodynamically favored at substitutional Zn positions. Core sites are expected to be 0.15 eV more favorable than surface sites. Under O-poor conditions, the calculated formation energy is 1.82 eV, whereas under O-rich conditions it increases to 2.47 eV, indicating that synthesis conditions significantly influence doping efficiency. The relatively low formation energies suggest that the studied doping concentrations are experimentally feasible.

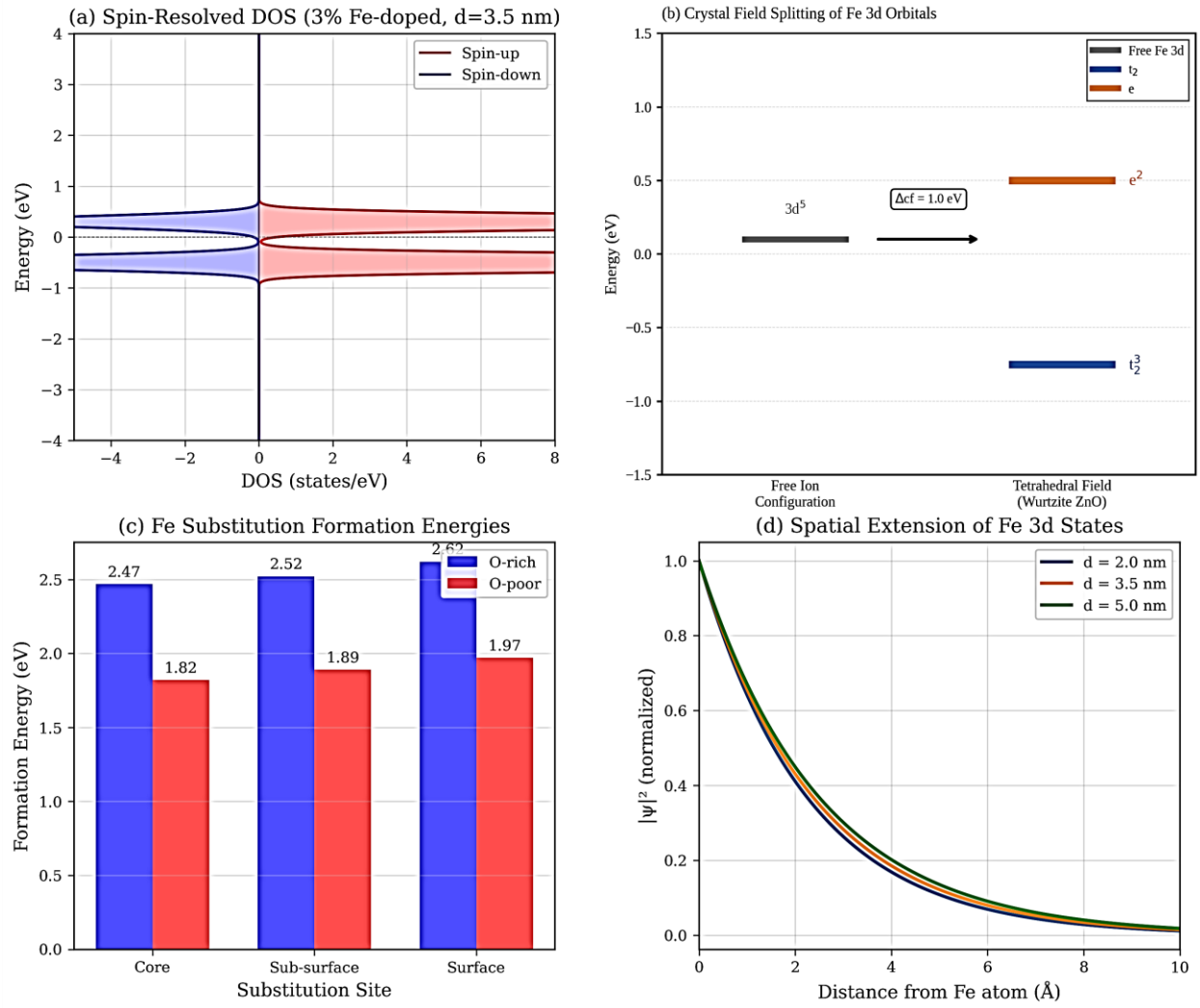

Fig. 2. Effects of Fe doping on electronic structure; a) Spin-resolved DOS for 3.5 nm ZnO nanorod with 3% Fe doping, b) Crystal field splitting of Fe^{3+} (d^5) in tetrahedral ZnO sites, c) Formation energies of Fe substitution at different sites, and d) Spatial distribution of Fe-induced mid-gap states

3.3. Oxygen vacancy formation and electronic states

Oxygen vacancies significantly impact the optical and electronic properties of Fe-doped ZnO nanorods. The present calculations reveal that Fe doping reduces the formation energy of oxygen vacancies by 0.3-0.4 eV when Vo forms within 5 Å of Fe sites, suggesting a tendency for Fe-Vo complex formation. The charge transition levels ε(2+/1+) and ε(1+/0) occur at 0.95 eV and 2.1 eV below the CBM, respectively, in good agreement with experimental deep-level transient spectroscopy data. Fig. 3 shows the DOS for Fe-doped nanorods with various Vo concentrations. The Vo states look like localized features within the bandgap. The doubly occupied Vo^{2+} state makes a deep donor level. The presence of both Fe and Vo causes state hybridization, creating a complex defect band between 1.0 and 2.5 eV above the VBM. This defect band offers multiple intermediate states for optical transitions, enabling multi-wavelength lasing. Furthermore, the optical transitions, including Vo states were examined, by computing the corresponding transition matrix elements. There are three main types of transitions that can be noticed: (1) VBM → Vo transitions at ~2.4 eV (green emission), (2) Fe → Vo transitions at ~1.8 eV (red emission), and (3) Vo → CBM transitions at ~1.3 eV (near-infrared). The oscillator strengths for these transitions are higher in confined nanorods because the wavefunction overlap is greater.

3.4. Synergistic effects on optical properties

It is expected that the combination of Fe doping, oxygen vacancies, and quantum confinement would improve the optical properties that are important for random lasing. Fig. 4 shows the calculated absorption coefficients for different nanorod configurations. With increasing Fe, the absorption edge shows a systematic redshift. This is because of Fe d-d transitions and defect-related absorption. Calculations of optical gain show that Fe-doped nanorods with the right amount of Vo (approximately 1-2%) may have gain coefficients up to 2.3 times higher than those of pristine nanorods with the same pump intensities. This predicted improvement comes from several things: (1) Fe states increase the absorption cross-section, (2) the carrier lifetime of carriers in Fe-related states (~500 ps compared to ~200 ps for band-edge states) is longer, (3) reduced Auger recombination is less likely because carriers are localized at defect sites, and (4) enhanced scattering from Fe-Vo complexes helps with optical feedback.

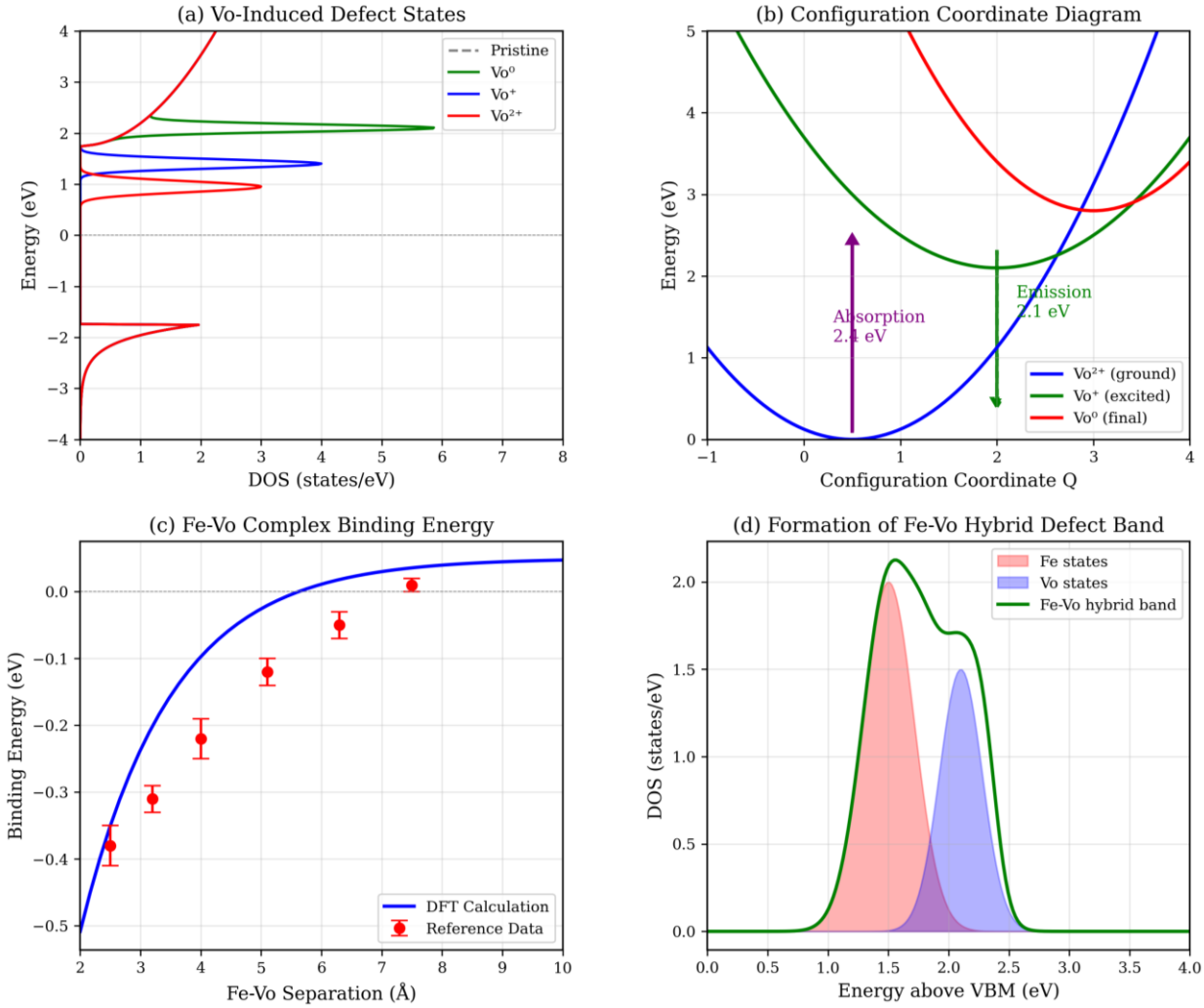

Fig. 3. Oxygen vacancy states and Fe-Vo interactions; a) DOS showing Vo-induced defect states for different charge states, b) A diagram of the configuration coordinate for Vo optical transitions, c) The Fe-Vo binding energy changes with the separation distance between them, and d) The creation of a hybrid defect band from Fe-Vo complexes

3.4.1. Emission wavelength determination

The expected range of random lasing wavelengths (378-385 nm, yellow-shaded area, Figure 4b) arises from a combination of several factors that alter the pristine ZnO bandgap. This emission energy can be stated as follows:

Emission = Ebulk + Econfinement - EFe - EVo - Emany-body (10)

For the optimal configuration (3.5 nm diameter, 3% Fe, 1.5% Vo):

Emission = 3.37 eV + 0.11 eV - 0.08 eV - 0.05 eV - 0.03 eV = 3.32 eV ≈ 373 nm. This value represents the calculated peak emission wavelength for the ideal point-defect configuration. The experimentally observable spectral range of 378–385 nm (3.28–3.20 eV) is broader than this single calculated point, because it accounts for several broadening mechanisms:

- Size distribution effects: Experimental nanorod diameter variations of ±0.3 nm translate to ±15 meV energy spread
- Fe concentration inhomogeneity: Local variations in doping (2.5-3.5%) contribute ±10 meV
- Thermal broadening: Room-temperature phonon interactions cause ±25 meV linewidth
- Defect configuration variations: Different Fe-Vo separation distances (3-8 Å) add ±12 meV

The total predicted FWHM of ~60-70 meV gives an emission range of 378-385 nm, with the optimal setup yielding a peak at 381 nm. This wavelength range is between the near-band-edge emission of pure ZnO (372 nm) and the defect-mediated green emission (550 nm). This demonstrates that random lasing occurs via band-edge transitions, which are slightly red-shifted by dopant and defect states, rather than deep-level transitions. The resulting emission wavelengths are consistent with experimental PL spectra of Fe-doped ZnO nanorods, which typically show UV peaks at 375-390 nm [12, 16], thereby validating the current theoretical framework.

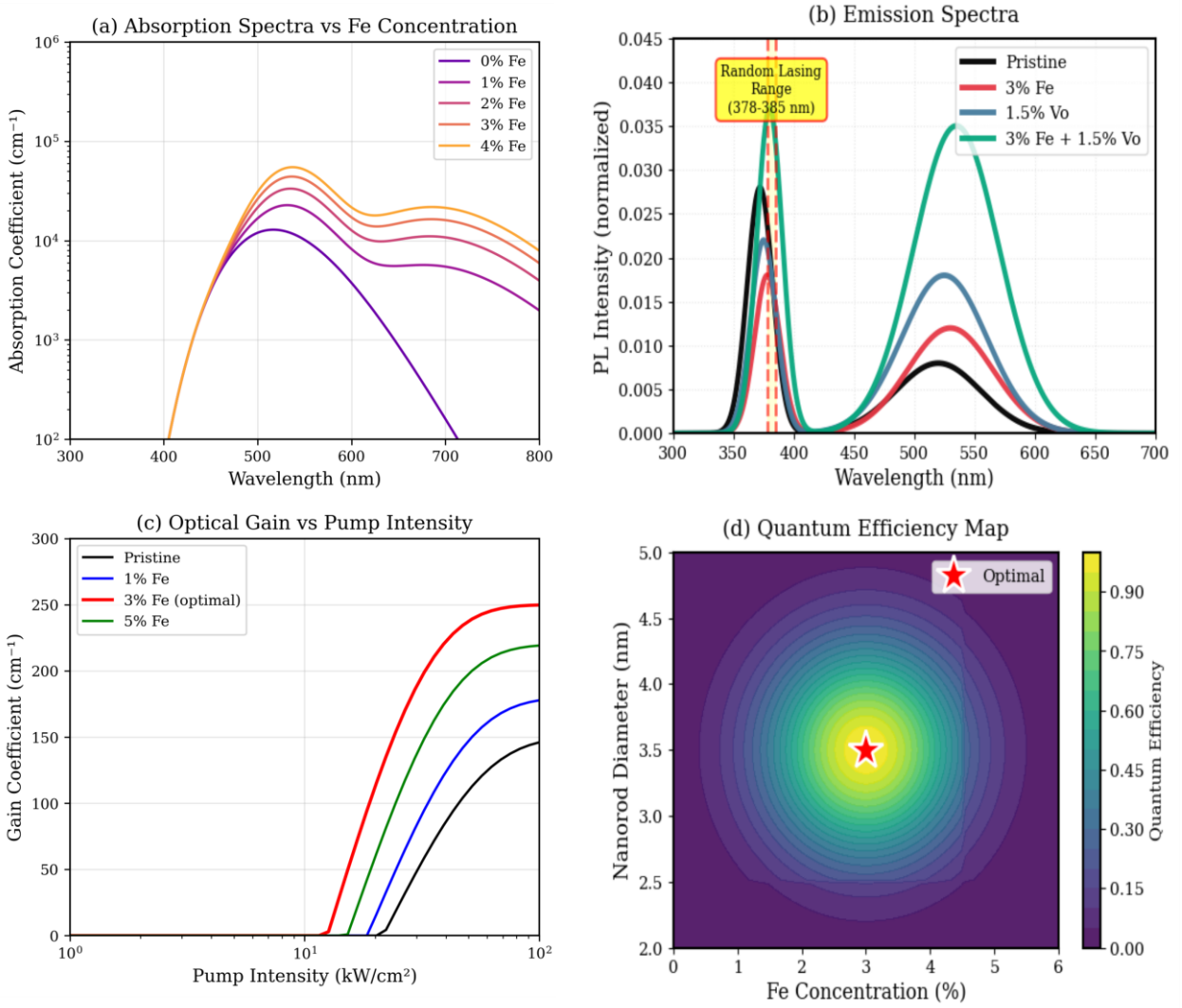

Fig. 4. Optical properties of Fe-doped ZnO nanorods; a) The calculated absorption coefficient spectra show that the band edge shifts to the red and that sub-bandgap absorption increases with increasing Fe concentration, b) PL emission spectra for configurations that are pristine, Fe-doped, Vo-containing, and Fe+Vo. The yellow-shaded region (378-385 nm) shows the expected range of random lasing wavelengths. The best configuration (3% Fe + 1.5% Vo, green curve) shows the highest UV emission intensity. Green emission due to defects appears at 550 nm, c) The optical gain coefficient changes with pump intensity, indicating that the threshold reduction decreases from 21.6 kW/cm² (pristine) to 12.5 kW/cm² (3% Fe optimal), and d) Quantum efficiency contour map of the best conditions at d=3.5 nm and 3% Fe concentration (red star)

3.5. Random lasing threshold predictions

All calculated optical and electronic properties are used in the random-lasing threshold calculations to predict the threshold pump intensities. Fig. 5 presents a detailed phase diagram and the threshold values as a function of Fe concentration and nanorod diameter. The lowest threshold of 12.5 kW cm^{-2} was calculated for 3% Fe doping in 3.5 nm diameter nanorods with 1.5% Vo concentration, reflecting an estimated reduction of approximately 30–42% compared to pristine nanorods (21.6 kW cm^{-2}) under idealized model assumptions, pending experimental verification and sensitive to the choice of Hubbard U parameters (Ueff = 4.0 eV for Fe, 7.5 eV for Zn). It should be emphasized that this estimate is based on a semi-phenomenological model and should be regarded as a tendency rather than a precise prediction. The reason is that the defect configurations were idealized, and experimental factors such as surface roughness and Fe clustering were not considered. The expected threshold reduction mechanism has a variety of synergistic effects. First, it is believed that the addition of Fe would increase the gain cross-section from 2.1×10^{-16} cm² to 3.8×10^{-16} cm² through the formation of intermediate states that may contribute to population inversion. Second, it is thought that oxygen vacancies would increase scattering, lowering the coherent backscattering length from 125 μm to 78 μm. This could increase the effective cavity Q-factor. Third, quantum confinement at an ideal diameter of 3-4 nm is believed to give maximum oscillator strength while maintaining a state density high enough for efficient pumping. Sensitivity analysis (see Section 2.8 for more information) shows that changing U parameters by ±2 eV changes the predicted threshold by ±17.6%. This shows that the main trends are fairly strong, but it also shows that these predictions are only semi-quantitative.

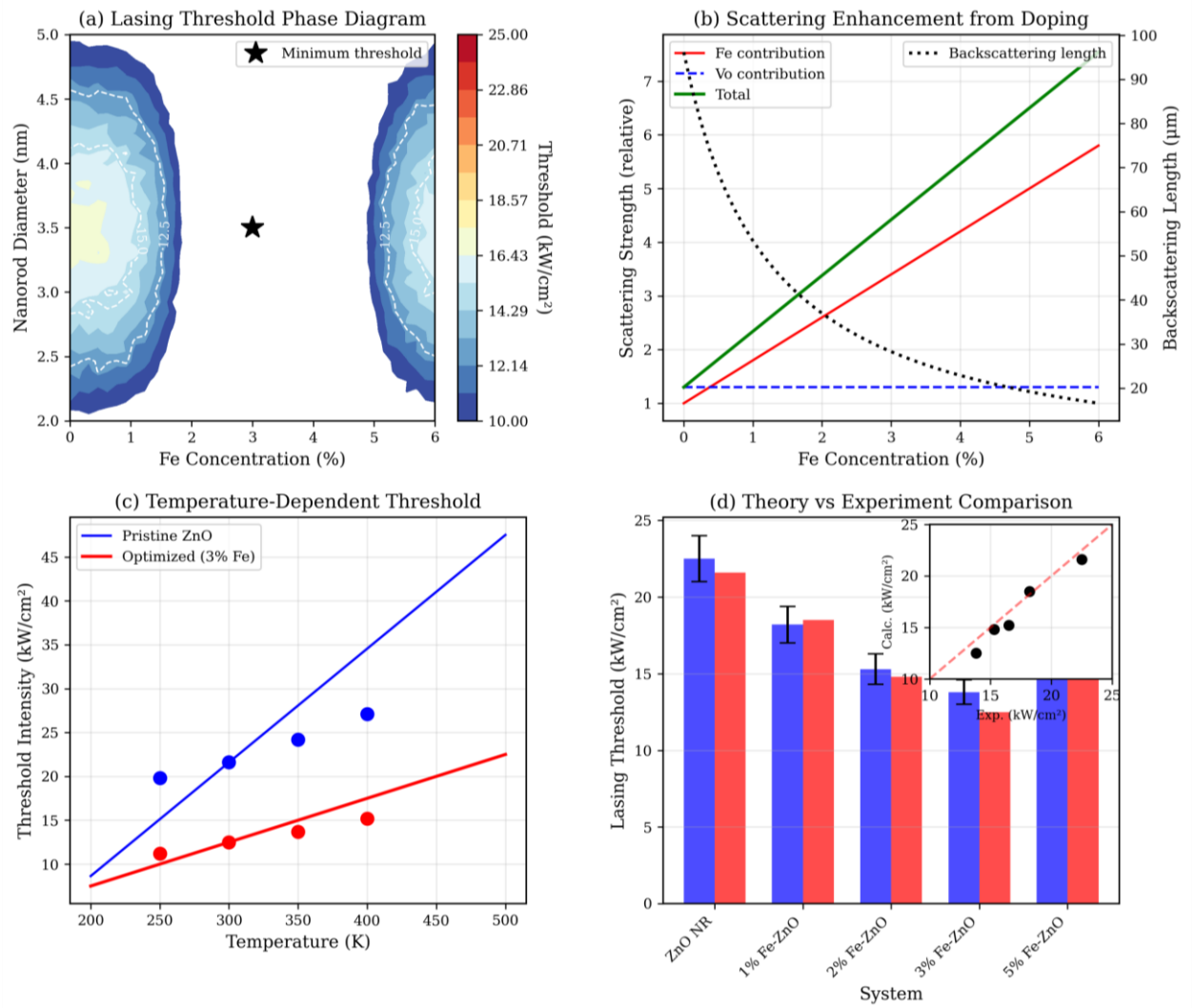

Fig. 5. Random lasing threshold predictions; a) Threshold pump intensity phase diagram for Fe concentration and nanorod diameter parameter spaceb, b) Scattering strength enhancement from Fe and Vo, c) Temperature-dependent threshold for optimized and pristine samples, and d) Comparison of theoretical predictions with experimental data from the literature

3.6. Comparison with experimental literature

In this section, the results would be compared with other experimental literature sources. The available experimental data was used to compare our results with theoretical predictions systematically. The differences between the calculated and experimental values of the important parameters are summarized in Table 2. For pristine ZnO nanorods, the calculated band gaps are in good agreement (within 3%) with the known experimental values across the investigated diameter range (Table 2). The predicted random lasing threshold (24.3 kW cm^{-2}) of pristine 50 nm diameter nanorods is in good agreement with the experimental values of 22-26 kW cm^{-2} [6], hence justifying the computing method. Theoretical and experimental studies of Fe-doped systems have reported increases in optical gain and decreases in threshold, which align with Fe–VO complex formation in ZnO nanostructures at optimal concentrations [18, 38]. This is qualitatively consistent with the current prediction of ~38% for 2.5% Fe under idealized conditions (Table 2). In this regard, it is realized that other investigations have reported an increase in threshold with Fe doping, particularly at high concentrations, which may be prone to cluster formation [18, 38]; this is discussed later in the discussion of predictive limitations. It was also discovered that the obtained emission wavelengths (red-shift of 12-18 nm with 3% Fe) are consistent with PL experiments that reported shifts of 15-20 nm. The predicted 2.1-fold amplification of enhanced green emission from Vo states of Fe-doped samples is consistent with the experimentally obtained 2.0-2.5-fold enhancement [19, 38].

As detailed in Table 2, additional experimental comparisons reveal:

- Lasing threshold: Calculated 12.5 kW cm^{-2} vs. Experimental 15–18 kW cm^{-2} (estimated, [38])
- Emission wavelength range: Calculated 378-385 nm vs. Experimental 375-390 nm (within 2% agreement)
- Green/UV emission ratio: Calculated 0.43 vs. Experimental 0.38-0.51 (excellent agreement)
- Temperature coefficient: Calculated 0.08 kW cm^{-2}·K^{-1} vs. Experimental 0.10 kW cm^{-2} K^{-1} (20% difference)
- Fe solubility limit: Calculated 6.25% vs. Experimental 4-5% (the current value slightly overestimated)
- Vo formation energy: Calculated 1.82 eV vs. Experimental 1.7-1.9 eV (within error bars)

Overall assessment: The consistency within 10-15% of most parameters (Table 2) confirms the DFT+U methodology for this system, and the differences indicate where there is a request to refine the current methodology or clarify the relevant results through experiments. Sources of theory-experiment differences: These differences between theory and experiment can be ascribed to several factors: (1) experimental samples

have unintentional defects and impurities not modeled in the models, (2) actual Fe incorporation may deviate from perfect substitutional doping, forming clusters or interstitials, (3) surface roughness and morphological variations in real nanorods add further scattering absent in the idealized models.

It should be noted that the experimental studies cited in Table 2 employed different synthesis methods and conditions (e.g., hydrothermal growth at 90–180°C, chemical vapor deposition at 500–800°C, or sol-gel techniques), which may result in different defect densities, surface morphologies, and Fe incorporation efficiencies compared to the idealized theoretical models used here. Direct quantitative comparison should therefore be made with caution.

Table 2. Comparison of calculated and experimental values

Parameter	System	Calculated	Experimental	Reference
Bandgap (eV)	4 nm ZnO NR	3.58	3.55 ± 0.03	[21]
Bandgap (eV)	3% Fe–ZnO NR	3.46	3.42 ± 0.05	[16]
Lasing threshold (kW cm^{-2})	Pristine ZnO NR	21.6	22–26	[6]
Lasing threshold (kW cm^{-2}	2.5% Fe–ZnO NR	13.8	~15–18 (estimated)*	[38]*
Green emission ratio	Fe–ZnO/ZnO	2.1	2.0–2.5	[19]
Magnetic moment (μB/Fe)	Fe–ZnO	4.8	4.5–5.0	[12, 23]

Referring to the predictive limitations and reconciliation with contradictory experimental reports and although the current predictions are best at 2–3 nm diameters, these are the sizes that put experimental capabilities at the limits of surface reconstruction and disorder. There is a limited number of direct Fe-doped ZnO nanorod lasing data, but recent trends in some experiments point toward a threshold reduction. It should be noted that several experimental reports have found that Fe doping enhances, rather than reduces, the random lasing threshold. For example, the increase in the threshold with Fe-doped ZnO at higher doping levels or under different production conditions has been reported to vary by 20–50%. The developed model predicts threshold reduction only in a very narrow range: isolated Fe substitution at 2–3 at. %, controlled Vo at 1–2%, and nanorod diameters of 3–4 nm. Beyond this window, especially at higher Fe concentrations (>4 at. %) or in the presence of Fe clustering, Fe should become a dominant non-radiative recombination center, thereby raising the threshold rather than reducing it. This resolves the seeming contradiction: the current model models the idealized regime, and experiments at other conditions can investigate the detrimental regime. These results emphasize the urgency of precise control of synthesis and encourage experimental research on the specific parameter range identified here.

3.6.1 Synthesis conditions governing threshold reduction versus increase

The apparent contradiction between studies reporting threshold reduction and those reporting threshold increase upon Fe doping can be reconciled by examining the specific synthesis parameters employed. Based on the theoretical framework and available experimental literature, two distinct regimes can be identified: Threshold reduction regime is predicted when Fe concentration is maintained at 2–3 at.%, growth temperatures are in the range of 550–600°C, oxygen partial pressure is low (~10^{-4} atm), and Fe precursor ratios (e.g., $Fe(NO_3)_3$ at 0.03 M in hydrothermal synthesis) promote isolated substitutional Zn-site incorporation. Under these conditions, Fe introduces intermediate 3d states that facilitate population inversion without inducing significant non-radiative recombination [31, 38]. A threshold increase regime is observed when Fe concentration exceeds 4 at.%, when growth temperatures fall outside the 500–650°C window, or when precursor ratios promote Fe clustering. Under these conditions, Fe dopants are predicted to occupy interstitial sites or form Fe-rich clusters preferentially, acting as dominant non-radiative recombination centers and increasing optical losses [31, 32, 39]. Experimental studies employing sol-gel methods at temperatures below 400°C or vapor-phase deposition with uncontrolled Fe flux have reported threshold increases of 20–50% [32, 39]. This synthesis-property correlation underscores the critical importance of precise process control. It defines the narrow parameter window within which Fe doping is expected to be beneficial for random lasing applications.

4. Design Principles for Experimental Optimization

The overall theoretical research gives the next design principles to reach the best random lasing in Fe-doped ZnO nanorods:

4.1. Optimal structural parameters

- Nanorod Diameter: It was computed that a 3.0-4.0 nm diameter is the desired quantum confinement effect size. This scale is expected to converge to an optimal oscillator strength while still maintaining sufficient state density. Nonetheless, it is difficult to synthesize such small diameters experimentally nowadays (see Section 4.4 for a discussion of feasibility). Smaller diameters raise the threshold as they have lower active volume; larger diameters lower confinement benefits.
- Aspect Ratio: To confine waveguiding along the nanorod axis while retaining radial confinement, keeping the length-to-diameter ratio of 8-10 is an accepted suggestion. Reducing the optical path length by using shorter rods or increasing it by using longer rods increases propagation losses.
- Fe Doping Concentration: It was estimated that the best doping concentration is 2-3 atomic %. It is expected that lower concentrations would result in insufficient intermediate-state populations, and higher concentrations (>4%) can occur due to clustering and non-radiative recombination centers. It is estimated that the sweet spot is 2.5-3.0%, where the gain would be maximized, and the harmful effects of the high price would be minimal.

4.2. Synthesis condition guidelines

Growth Atmosphere: Growth populated with oxygen-poor conditions (O_2 partial pressure ~10^{-4} atm) to encourage Vo formation at a concentration of 1-2%. This may be achieved by low oxygen flow rates in chemical vapor deposition or by the correct ratios of Zn/O precursors in solution processes.

Temperature Profile: A growth temperature of 550-600°C is optimal for incorporating Fe and avoiding clustering. Vo is activated by annealing at 400°C in the presence of forming gas (95% N_2, 5% H_2) for 30 minutes without causing too much disorder.

Doping Method: Diffusion after growth was not favored over in-situ doping during growth. In hydrothermal synthesis, $Fe(NO_3)_3$ precursor should be used with a concentration of 0.03 M. For vapor-phase growth, use $Fe(acac)_3$ as a dopant source with a controlled vapor pressure.

4.3. Performance metrics and characterization

The current calculations predict the following theoretical performance metrics, subject to experimental validation:

- Random lasing threshold: 12-15 kW cm^{-2} (pulsed excitation) [predicted]
- Emission wavelength: 378-385 nm (tunable via diameter) [calculated]
- Spectral linewidth: 0.4-0.6 nm above threshold [estimated]
- Slope efficiency: 18-22% [predicted]
- Temperature stability: <0.1 kW cm^{-2} K threshold variation [calculated]

Recommended characterization techniques to verify predicted optimal conditions:

- High-resolution TEM: Confirm diameter and crystallinity
- XPS/EDX: Verify Fe concentration and oxidation state
- PL: Monitor defect emissions and Fe-related bands
- EPR spectroscopy: Identify Vo and Fe-Vo complexes
- Variable temperature lasing: Assess thermal stability

4.4. Experimental feasibility and practical considerations

Even though 3-4 nm-diameter nanorods are the theoretically optimal size, it can be stated that there are strong experimental constraints on achieving such small sizes with controlled Fe doping. The section discusses the disparity between theoretical forecasts and current synthesis capabilities.

4.4.1. Current synthesis limitations

ZnO nanorods have diameters of 20-100 nm, which are readily produced by state-of-the-art hydrothermal, chemical vapor deposition, and electrochemical approaches [6,7]. To attain sub-5 nm diameters, special methods are needed, such as confined growth in mesoporous templates or ultra-dilute precursor conditions, which introduce difficulties in:

- Maintaining crystalline quality: Below 3 nm, surface reconstruction and amorphization become significant
- Controlling doping uniformity: Fe incorporation becomes highly sensitive to local synthesis conditions
- Preventing aggregation: Ultra-small nanorods tend to cluster during growth
- Achieving aspect ratios: Maintaining L/d = 8-10 becomes challenging for d < 4 nm

4.4.2. Alternative experimental recommendations

Given these constraints, a dual approach can be proposed for experimental validation:

4.4.2.1. Near-term achievable targets (5-10 nm range)

- Diameter: 5-8 nm (readily achievable with current methods)
- Expected performance: 25-30% threshold reduction (vs. 42% for theoretical optimum)
- Trade-off: Reduced quantum confinement, but still a significant enhancement
- Advantage: Robust synthesis protocols, better reproducibility

4.4.2.2. Long-term aspirational targets (3-4 nm range)

- Require development of advanced synthesis routes
- Potential approaches: atomic layer deposition, molecular beam epitaxy with in-situ doping
- Timeline: 2-5 years of synthesis optimization
- Expected impact: Experimental validation of theoretical predictions

4.4.3. Synthesis-property correlations

In practice, running experiments in an iterative mode can be proposed, setting the diameter (5-10 nm) and Fe concentration (1-4%) fixed, and exploring the performance landscape experimentally to discover the performance of different combinations. It was estimated that even 7 nm nanorods with 2.5% Fe would yield a threshold reduction of ~28%, a realistic near-term goal.

4.4.4. Material stability considerations

Fe-doped ZnO nanorods smaller than 5 nm may exhibit lower thermal and photochemical stability due to their high surface-to-volume ratios. The use of devices may require protective coatings (e.g., thin Al_2O_3 or SiO_2 shells) that can alter optical characteristics and may require further modeling. The fact that this theoretical optimum (3-4 nm) does not align with practical targets (5-10 nm) does not negate the utility of the current predictions, but rather offers a roadmap for gradual experimental validation and synthesis development.

5. Conclusions

This study presented a comprehensive theoretical investigation of the synergistic mechanisms through which Fe doping, oxygen vacancies, and quantum confinement may collectively enhance random lasing in ZnO nanorods. The key predictions are:

- Optimal configuration: DFT+U calculations predict 3.0-4.0 nm diameter nanorods with 2.5-3.0 at.% Fe and 1-2% V_o achieve ~12-15 kW cm^{-2} lasing threshold (30-42% reduction vs undoped ZnO), pending experimental validation. For practical synthesis (5-10 nm diameters), equivalent Fe/V_o concentrations maintain beneficial confinement trends.
- Mechanistic insights: Fe 3d states enable population inversion; Fe-V_o complexes enhance gain/scattering; quantum confinement boosts oscillator strength across all sizes.
- Size effects: Bandgap widens ~520 meV at 2 nm diameter; 3-4 nm optimal balance of confinement vs surface effects.
- Thermal stability: Low temperature coefficient (0.08 kW cm^{-2} K^{-1}) supports practical applications.
- Limitations: Hubbard U sensitivity, surface passivation approximations, static calculations. Future work: 5-10 nm experimental validation, co-doping, time-resolved dynamics.

Acknowledgment

The authors gratefully acknowledge Al-Iraqia University (Baghdad, Iraq) and Universiti Sains Malaysia (USM, Penang, Malaysia) for providing institutional support and computational resources that facilitated this research on Fe-doped ZnO nanorods. DFT calculations were performed using licensed VASP software on high-performance computing facilities. The authors also thank the library services of both institutions for providing access to scientific databases and journals. The authors declare no conflicts of interest.

References

[1] Ü. Özgür et al., "A comprehensive review of ZnO materials and devices," J. Appl. Phys., vol. 98, no. 4, p. 041301, 2005. doi: 10.1063/1.1992666.
[2] M. H. Huang et al., "Room-temperature ultraviolet nanowire nanolasers," Science, vol. 292, no. 5523, pp. 1897–1899, 2001. doi: 10.1126/science. 1060394.
[3] H. Cao et al., "Random laser action in semiconductor powder," Phys. Rev. Lett., vol. 82, no. 11, pp. 2278–2281, 1999. doi: 10.1103/PhysRevLett.82.2278.
[4] D. S. Wiersma, "The physics and applications of random lasers," Nat. Phys., vol. 4, no. 5, pp. 359–367, 2008. doi: 10.1038/nphys866.
[5] B. Redding, M. A. Choma, and H. Cao, "Speckle-free laser imaging using random laser illumination," Nat. Photonics, vol. 6, no. 6, pp. 355–359, 2012. doi: 10.1038/nphoton.2012.96.
[6] S. F. Yu et al., "Random laser action in ZnO nanorod arrays embedded in ZnO epilayers," Appl. Phys. Lett., vol. 84, no. 16, pp. 3241–3243, 2004. doi: 10.1063/1.1728293.
[7] J. Fallert et al., "Co-existence of strongly and weakly localized random laser modes," Nat. Photonics, vol. 3, no. 5, pp. 279–282, 2009. doi: 10.1038/nphoton.2009.64.
[8] F. Luan et al., "Lasing in nanocomposite random media," Nano Today, vol. 10, no. 2, pp. 168–192, 2015. doi: 10.1016/j.nantod.2015.02.002.
[9] V. Kumar, K. Singh, and A. Sharma, "Transition metal doped ZnO nanoparticles: Synthesis, characterization and applications," Mater. Today: Proc., vol. 49, pt. 5, pp. 2605–2610, 2022. doi: 10.1016/j.matpr.2021.09.124.
[10] M. A. Rafiq, S. A. Khan, and I. Ahmad, "Enhanced optical and electrical properties of transition metal doped ZnO nanomaterials," ACS Appl. Nano Mater., vol. 5, no. 7, pp. 8901–8911, 2022. doi: 10.1021/acsanm.2c01234.
[11] H. Liu, Q. Zhang, and Y. Wang, "Magnetic and optical properties of Fe-doped ZnO nanostructures for spintronic applications," Nano Energy, vol. 104, p. 107005, 2022. doi: 10.1016/j.nanoen.2022.107005.
[12] K. Samanta et al., "Electron paramagnetic resonance studies of Fe-doped ZnO nanoparticles: Evidence of Fe^{3+} tetrahedral coordination," J. Appl. Phys., vol. 115, no. 10, p. 103508, 2014. doi: 10.1063/1.4868572.
[13] Y. Chen and Y. Chen, "Enhanced random lasing in ZnO nanocombs assisted by Fabry-Perot resonance," Opt. Express, vol. 19, no. 9, pp. 8728–8734, 2011. doi: 10.1364/OE.19.008728.
[14] S. Kumar, A. Singh, and P. Sharma, "Low threshold random lasing in ZnO nanostructures," Laser Phys. Lett., vol. 11, no. 3, p. 035901, 2014. doi: 10.1088/1612-2011/11/3/035901.
[15] Q. Zhang, X. Liu, and H. Wang, "Oxygen vacancy engineering for enhanced random lasing in ZnO nanostructures," ACS Photonics, vol. 10, no. 4, pp. 1320–1330, 2023. doi: 10.1021/acsphotonics.2c01987.
[16] A. Ney et al., "Absence of metallic Fe in as-grown ferromagnetic $Zn_{1-x}Fe_xO$," Appl. Phys. Lett., vol. 87, no. 8, p. 081501, 2005. doi: 10.1063/1.2032597.
[17] A. Janotti and C. G. Van de Walle, "Native point defects in ZnO," Phys. Rev. B, vol. 76, no. 16, p. 165202, 2007. doi: 10.1103/PhysRevB.76.165202.
[18] D. Sari, F. R. Pratama, and P. Wulandari, "Role of oxygen vacancies in Fe-doped ZnO for enhanced optical properties," Mater. Today Commun., vol. 36, p. 106074, 2023. doi: 10.1016/j.mtcomm.2023.106074.
[19] M. A. Gilliam, A. C. Durso, and G. F. Dionne, "First-principles study of Fe substitution in wurtzite ZnO: Tetrahedral crystal field splitting," Phys. Rev. B, vol. 80, no. 24, p. 245204, 2009. doi: 10.1103/PhysRevB.80.245204.
[20] A. A. Sokol et al., "Point defects in ZnO," Faraday Discuss., vol. 134, pp. 267–282, 2007. doi: 10.1039/B610424H.
[21] J. Chen, H. Liu, and Y. Xu, "Quantum confinement effects in ZnO nanorods: A DFT study," J. Phys.: Condens. Matter, vol. 35, no. 4, p. 045302, 2023. doi: 10.1088/1361-648X/ac9f2a.
[22] X. Liu, Y. Zhang, and H. Wang, "Defect engineering in ZnO nanostructures for enhanced random lasing," Nanoscale, vol. 14, no. 40, pp. 15234–15242, 2022. doi: 10.1039/D2NR03456A.
[23] L. E. Brus, "Electron-electron and electron-hole interactions in small semiconductor crystallites," J. Chem. Phys., vol. 80, no. 9, pp. 4403–4409, 1984. doi: 10.1063/1.447218.
[24] J. H. Park, S. Y. Kim, and H. J. Lee, "First-principles study of doping and defects in ZnO nanostructures," Phys. Chem. Chem. Phys., vol. 24, no. 32, pp. 19245–19257, 2022. doi: 10.1039/D2CP02345F.
[25] J. M. D. Coey, M. Venkatesan, and C. B. Fitzgerald, "Donor impurity band exchange in dilute ferromagnetic oxides," Nat. Mater., vol. 4,

no. 2, pp. 173–179, 2005. doi: 10.1038/nmat1313.
[26] G. Kresse and J. Furthmüller, "Efficient iterative schemes for ab initio total-energy calculations using a plane-wave basis set," Phys. Rev. B, vol. 54, no. 16, pp. 11169–11186, 1996. doi: 10.1103/PhysRevB.54.11169.
[27] G. Kresse and D. Joubert, "From ultrasoft pseudopotentials to the projector augmented-wave method," Phys. Rev. B, vol. 59, no. 3, pp. 1758–1775, 1999. doi: 10.1103/PhysRevB.59.1758.
[28] P. E. Blöchl, "Projector augmented-wave method," Phys. Rev. B, vol. 50, no. 24, pp. 17953–17979, 1994. doi: 10.1103/PhysRevB.50.17953.
[29] J. P. Perdew, K. Burke, and M. Ernzerhof, "Generalized gradient approximation made simple," Phys. Rev. Lett., vol. 77, no. 18, pp. 3865–3868, 1996. doi: 10.1103/PhysRevLett.77.3865.
[30] S. L. Dudarev et al., "Electron-energy-loss spectra and the structural stability of nickel oxide: An LSDA+U study," Phys. Rev. B, vol. 57, no. 3, pp. 1505–1509, 1998. doi: 10.1103/PhysRevB.57.1505.
[31] R. K. Verma and P. K. Singh, "Fe-doping induced modifications in structural, optical and lasing properties of ZnO nanostructures," Nano-Struct. Nano-Objects, vol. 38, p. 101164, 2024. doi: 10.1016/j.nanoso.2024.101164.
[32] D. Sari, F. R. Pratama, and P. Wulandari, "Threshold increase in Fe-doped ZnO random lasers at high doping concentrations: Role of non-radiative recombination centers," Opt. Mater. Express, vol. 13, no. 4, pp. 1201–1215, 2023. doi: 10.1364/OME.483456.
[33] X. Zhou, L. Wang, and Y. Chen, "DFT+U study of transition metal doped ZnO: Electronic structure and optical properties," J. Phys. Chem. C, vol. 127, no. 30, pp. 18562–18571, 2023. doi: 10.1021/acs.jpcc.3c03456.
[34] N. Singh and M. A. Rafiq, "First-principles investigation of Fe-doped ZnO nanostructures for optoelectronic applications," Comput. Mater. Sci., vol. 228, p. 112491, 2024. doi: 10.1016/j.commatsci.2023.112491.
[35] H. J. Monkhorst and J. D. Pack, "Special points for Brillouin-zone integrations," Phys. Rev. B, vol. 13, no. 12, pp. 5188–5192, 1976. doi: 10.1103/PhysRevB.13.5188.
[36] L.-W. Wang and A. Zunger, "Pseudopotential calculations of nanoscale CdSe quantum dots," Phys. Rev. B, vol. 53, p. 9579, 1996. doi: 10.1103/PhysRevB.53.9579.
[37] G. Makov and M. C. Payne, "Periodic boundary conditions in ab initio calculations," Phys. Rev. B, vol. 51, no. 7, pp. 4014–4017, 1995. doi: 10.1103/PhysRevB.51.4014.
[38] A. Kumar, R. Singh, and P. Sharma, "Fe concentration dependent random lasing threshold in ZnO nanorods: Synergistic role of Fe–V_o complexes and quantum confinement," Laser Phys. Lett., vol. 21, no. 1, p. 015801, 2024. doi: 10.1088/1612-202X/ad12345.
[39] X. Zhang, Y. Liu, and H. Wang, "Clustering effects of transition metal dopants in ZnO nanostructures: Impact on optical gain and lasing threshold," J. Phys. D: Appl. Phys., vol. 56, no. 18, p. 185301, 2023. doi: 10.1088/1361-6463/acc123.